International Journal of Applied Earth Observation and Geoinformation 13 (2011) 812–818

Contents lists available at ScienceDirect

International Journal of Applied Earth Observation and Geoinformation

journal homepage: www.elsevier.com/locate/jag

Monitoring of urban subsidence with SAR interferometric point target analysis: A case study in Suzhou, China

Yonghong Zhang[a,*], Jixian Zhang[a], Hongan Wu[a], Zhong Lu[b], Sun Guangtong[a]

[a] Chinese Academy of Surveying and Mapping, 28 Lianhuachixi Road, Haidian district, Beijing 100830, PR China
[b] USGS EROS Center & Cascades Volcano Observatory, 1300 SE Cardinal Ct., Bldg. 10, Ste. 100, Vancouver, WA 98683-9589, United States

ARTICLE INFO

Article history:
Received 13 September 2010
Accepted 13 May 2011

Keywords:
SAR
Interferometric point target analysis
Ground subsidence
Monitoring

ABSTRACT

Ground subsidence, mainly caused by over exploitation of groundwater and other underground resources, such as oil, gas and coal, occurs in many cities in China. The annual direct loss associated with subsidence across the country is estimated to exceed 100 million US dollar. Interferometric SAR (InSAR) is a powerful tool to map ground deformation at an unprecedented level of spatial detail. It has been widely used to investigate the deformation resulting from earthquakes, volcanoes and subsidence. Repeat-pass InSAR, however, may fail due to impacts of spatial decorrelation, temporal decorrelation and heterogeneous refractivity of atmosphere. In urban areas, a large amount of natural stable radar reflectors exists, such as buildings and engineering structures, at which radar signals can remain coherent during a long time interval. Interferometric point target analysis (IPTA) technique, also known as persistent scatterers (PS) InSAR is based on these reflectors. It overcomes the shortfalls in conventional InSAR. This paper presents a procedure for urban subsidence monitoring with IPTA. Calculation of linear deformation rate and height residual, and the non-linear deformation estimate, respectively, are discussed in detail. Especially, the former is highlighted by a novel and easily implemented 2-dimensional spatial search algorithm. Practically useful solutions that can significantly improve the robustness of IPTA, are recommended. Finally, the proposed procedure is applied to mapping the ground subsidence in Suzhou city, Jiangsu province, China. Thirty-four ERS-1/2 SAR scenes are analyzed, and the deformation information over 38,881 point targets between 1992 and 2000 are generated. The IPTA-derived deformation estimates correspond well with leveling measurements, demonstrating the potential of the proposed subsidence monitoring procedure based on IPTA technique. Two shortcomings of the IPTA-based procedure, e.g., the requirement of large number of SAR images and assumed linear plus non-linear deformation model, are discussed as the topics of further research.

1. Introduction

Ground subsidence at relatively large amplitude has started in several coastal cities in China in 1980s, such as Shanghai and Tianjing. Following fast economy developments across the country, ground subsidence has expanded into inland areas. The main causes of ground subsidence in China are over exploitation of groundwater and other underground resources, such as oil, gas and coal. The subsidence has not only affected individual metropolis but it has also evolved into regional disasters (Dou, 2005). Currently, four major subsidence zones exist across the country: the Beijing–Tianjing–Tangshan area, the Yangtze River delta region centered at Shanghai, Suzhou and Wuxi, the Pearl river delta region centered at Guangzhou and Zhuhai, and the Weihe–Fenhe basin centered at Xi'an and Taiyuan. The total area affected by ground subsidence up to 2003 was approximately 930,000 km^2, causing annual direct economic loss of over 1.2 billion US Dollar (Jin and Pan, 2007). Land subsidence has been recognized as a major threat to the country's sustainable development. Therefore reliable and effective solutions for monitoring and modeling have to be developed.

Traditionally, different ways exist to measure ground subsidence. Examples are spirit level, borehole extensometer and GPS. These methods measure vertical displacement at accuracy of several millimeters to 0.01 mm (Galloway et al., 2000). All these are ground-based measurements at sparse locations, however, and they cannot achieve a sufficiently high spatial density over large areas. Interferometric SAR (InSAR) is a relatively new technology emerged in late 1980s that can measure topography at an accuracy of meters (Zebker et al., 1994b) and ground surface deformation on the scale of centimeters under ideal conditions (Gabriel et al., 1989; Massonnet and Feigl, 1998). For ground subsidence measurements, InSAR can achieve an accuracy comparable to GPS, but at a higher

* Corresponding author. Tel.: +86 10 63880521; fax: +86 10 63880535.
E-mail address: yhzhang@casm.ac.cn (Y. Zhang).

0303-2434/$ – see front matter © 2011 Elsevier B.V. All rights reserved.
doi:10.1016/j.jag.2011.05.003

spatial density and a larger coverage. InSAR has been successfully applied to monitor large-amplitude (i.e., large phase gradient) deformation episodes such as those caused by volcanoes and earthquakes (Massonnet et al., 1993, 1995; Zebker et al., 1994a; Lu et al., 2005, 2007). Due to temporal and spatial decorrelation, however, InSAR can encounter difficulties in mapping slow-evolving, long-lasting deformations such as subsidence (Mora et al., 2003). To cope with this, advanced InSAR algorithms, namely interferometric point target analysis (IPTA) (Werner et al., 2003) or permanent scatterers (PS) InSAR (Ferretti et al., 1999, 2001) have been proposed. IPTA deals with pixels associated with point-like targets. At those targets, the radar return is determined by dominant scatterers, which can stay stable for years. Therefore, the backscattered signals from these targets will remain coherent irrespective of the separation in time. Factors contributing to errors to deformation measurement will be estimated one by one by analyzing the interferometric phases in the time series at such point targets, resulting in an accurate deformation estimate.

This paper describes an operational procedure based on IPTA algorithm for urban subsidence monitoring. The procedure is characterized by two easily implemented solutions to two corresponding key processing issues in the IPTA algorithm: estimation of the linear deformation rate and digital elevation model (DEM) error, and the separation of atmospheric phase and non-linear deformation. These issues are introduced in Sections 2 and 3, respectively. Several important issues concerned with the success of the proposed procedure in practical applications are addressed in Section 4. Section 5 presents a case study of using IPTA to map ground subsidence in Suzhou city, Jiangsu province, China. Finally, discussion is given in Section 6.

2. Estimation of linear deformation and DEM error

IPTA requires a large stack of SAR images. Considering $K+1$ scenes of SAR data at single look complex (SLC) format where one is selected as the common master, and the rest is co-registered to the master. K interferograms will be formed. The criteria in the selection of the master image lies in considering the following aspects: the Doppler centroid should be near the average Doppler centroid of the $K+1$ images, the orbit should be near the geometric center of orbital tube spanned by available SAR images, it should have low atmospheric distortions, and the acquisition date should be close to the temporal average of the $K+1$ acquisitions. Next, point target candidates can be selected using coherence based or amplitude based method described by Ferretti et al. (2001).

Suppose that we have selected N point target candidates, and that the topography phase has been removed using existing DEMs, such as the SRTM DEM, from original interferometric phase. Then the differential interferometric phase of the ith point target in the kth interferogram can be expressed as:

$$\varphi_i^k = \mathrm{wrap}\{\varphi_{i,\mathrm{defo}}^k + \varphi_{i,\mathrm{atmo}}^k + \varphi_{i,\mathrm{noise}}^k + \varphi_{i,\mathrm{topo\text{-}res}}^k\} \quad (1)$$

where φ_i^k is the wrapped interferometric phase, $\varphi_{i,\mathrm{atmo}}^k$ is the phase associated with atmosphere heterogeneity (including the error related to inaccuracy of orbit determination which is discussed at a later stage), $\varphi_{i,\mathrm{defo}}^k$ is the phase due to deformation in the direction of Radar line-of-sight (LOS), $\varphi_{i,\mathrm{noise}}^k$ denotes the phase caused by decorrelation noise, and $\varphi_{i,\mathrm{topo\text{-}res}}^k$ describes the phase of residual topography, which is due to the errors of the DEM. Furthermore, the deformation phase can be divided into linear and nonlinear components (Ferretti et al., 1999; Mora et al., 2003)

$$\varphi_{i,\mathrm{defo}}^k = \frac{4\pi}{\lambda} t^k v_i + \varphi_{i,\mathrm{non\text{-}linear}}^k \quad (2)$$

where t^k is the time separation of the kth interferogram, λ the radar wavelength and v_i the linear deformation velocity.

The phase of residual topography has a linear dependence on DEM error with the ramp related to the normal baseline (Mora et al., 2003)

$$\varphi_{i,\mathrm{topo\text{-}res}}^k = a_1 B_{i,\perp}^k \Delta h_i \quad (3)$$

where $B_{i,\perp}^k$ is the normal baseline and Δh_i is the DEM error at the point target.

The phase variation between two neighboring point targets, e.g., points i, j equals

$$\Delta\varphi_{i,j} = \mathrm{wrap}\{a_1 B_{i,\perp}^k \Delta h_{i,j} + a_2 t^k \Delta v_{i,j} + \Delta\varphi_{i,j,\mathrm{res}}\} \quad (4)$$

where $a_2 = 4\pi/\lambda$. The phase model indicates a linear dependence on the perpendicular baseline with the slope corresponding to the relative DEM error between the two points, and a linear time dependence on the time interval of the interferogram with the slope corresponding to the relative deformation velocity. In addition to the two linear items, the phase model has a residual term $\Delta\varphi_{i,j,\mathrm{res}}$ which consists of the phase variation related to the relative difference of atmosphere artifacts (including orbital errors), nonlinear deformation and decorrelation noise between the neighboring point targets.

$$\begin{aligned}\Delta\varphi_{i,j,\mathrm{res}} &= \Delta\varphi_{i,j,\mathrm{non\text{-}linear}}^k + \Delta\varphi_{i,j,\mathrm{atmo}}^k + \Delta\varphi_{i,j,\mathrm{noise}}^k \\ &= \Delta\varphi_{i,j} - (a_1 B_{i,j,\perp}^k \Delta h_{i,j} + a_2 t^k \Delta v_{i,j})\end{aligned} \quad (5)$$

Eq. (4) indicates that the DEM error increment $\Delta h_{i,j}$ and deformation velocity increment $\Delta v_{i,j}$ between two neighboring points can easily be resolved by means of a two-dimensional (2D) regression analysis if the interferometric phase variation is unwrapped. Unfortunately, the phase variation from complex valued differential interferograms is still wrapped at this stage. Therefore we adopt a 2-D spatial searching algorithm to calculate the two unknown variables of the linear phase model and simultaneously conduct a phase unwrapping.

Since both the atmospheric phase and the nonlinear deformation phase are spatial low-pass signals, we may assume that

$$|\Delta\varphi_{i,j,\mathrm{res}}| < \pi \quad (6)$$

The following temporal coherence index is defined as

$$\gamma_{i,j} = \left| \frac{1}{K} \sum_{k=1}^{K} \exp(J\Delta\varphi_{i,j,\mathrm{res}}) \right| \quad (7)$$

where $J = \sqrt{-1}$.

Each item of $\exp(J\Delta\varphi_{i,j,\mathrm{res}})$ corresponds to a unit vector in complex plane, with $\Delta\varphi_{i,j,\mathrm{res}}$ as the main argument of the vector, if Eq. (6) holds. When the K unit vectors have similar main arguments as shown in Fig. 1(a), the average vector will be close to a unit vector and the temporal coherence index will be close to 1. When the main arguments of the K vectors are randomly distributed as shown in Fig. 1(b), the average will be zero. If the K unit vectors have similar main arguments then the linear phase model represented by $a_1 B_{i,j,\perp}^k \Delta h_{i,j} + a_2 t^k \Delta v_{i,j}$ fits the observations well, whereas K random main arguments indicate that the phase model was wrong. Therefore, we can set restricted variation ranges for $\Delta h_{i,j}$ and $\Delta v_{i,j}$, and search for the maximum $\gamma_{i,j}$ within the specified two-dimensional range with small sampling intervals. After obtaining appropriate solutions for $\Delta h_{i,j}$ and $\Delta v_{i,j}$, the unwrapped phase of $\Delta\varphi_{i,j}$ in Eq. (4) can be calculated directly.

Here we should note that Eq. (6) is a prerequisite for the success of the 2-D spatial search algorithm, and this is also true for other algorithms to calculate the relative linear deformation rate and DEM error, such as the periodogram method proposed by Ferretti

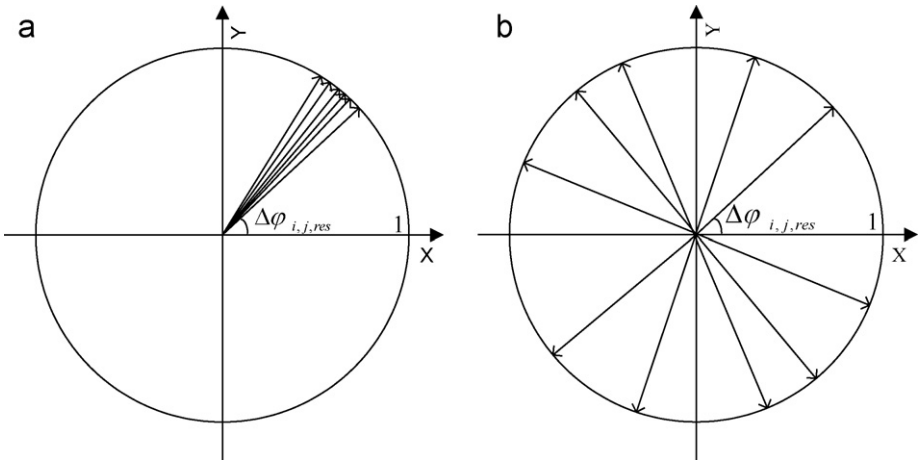

Fig. 1. *N* unitary vectors having (a) similar main arguments and (b) distributed main arguments. In the case of (a), the module of the sum of the *N* vectors is close to *N*; while in the case of (b), the sum of the *N* vectors is close to zero.

et al. (2000). If Eq. (6) does not hold, $\Delta\varphi_{i,j,\mathrm{res}}$ will be the argument of a unit vector, rather than the main argument. Thus there will be multiple solutions of $(\Delta h_{i,j}, \Delta v_{i,j})$ which can maximize the temporal coherence index. This means we may obtain wrong solutions of the phase model. Further discussion about this equation is given in Section 6.

The candidate point targets can be connected by means of triangulation. To make Eq. (6) hold, only those arcs of the triangles with distances below 2 km are considered for linear model calculation, since the correlation distance of atmosphere is estimated around 1–3 km (Hanssen, 2001). The results from the 2-D searching algorithm are relative values of DEM error and linear deformation rate between two points. With a good-quality reference point, at which the DEM error and linear deformation rate are known or assumed to be 0, the absolute values of the DEM error and linear deformation rate at each individual point can be derived by means of spatial integration (Mora et al., 2003).

3. Estimation of nonlinear deformation

After phase unwrapping and obtaining both the deformation rate and the DEM error, we consider the residual phase defined as:

$$\varphi^k_{i,\mathrm{res}} = \varphi^k_{i,\mathrm{unw}} - a_1 B^k_{i,\perp}\Delta h_i - a_2 t^k_i v_i = \varphi^k_{i,\text{non-linear}} + \varphi^k_{i,\mathrm{atmo}} + \varphi^k_{i,\mathrm{noise}} \quad (8)$$

where $\varphi^k_{i,\mathrm{unw}}$ is unwrapped interferometric phase.

The three components of the residual phase have different spatial and temporal characteristics. The atmospheric phase, $\varphi^k_{i,\mathrm{atmo}}$, is caused by the path delay heterogeneity at the two acquisition times of the interferogram. The atmospheric path delay is highly correlated in space, but varies randomly in time. The nonlinear deformation is generally low-pass in the temporal and spatial dimensions, but with a smaller correlation window size than atmospheric artifacts. The phase noise is random in both space and time.

The atmospheric phase of the master image is present in each of the interferogram stacks. To estimate the atmospheric phase for each interferogram, the atmospheric phase of the master image has to be estimated firstly.

The temporal average of the interferometric atmospheric phase is a good approximation of the atmospheric phase of the master image, given the large number of interferograms

$$\overline{\varphi}_{i,\mathrm{res}} = \sum_{k=1}^{K} \frac{\varphi^k_{i,\mathrm{atmo}}}{K} \quad (9)$$

Then the atmospheric phase of each interferogram will be given by

$$\varphi^k_{i,\mathrm{atm}} = \mathrm{lp\_space}\ (\mathrm{hp\_time}(\varphi^k_{i,\mathrm{res}} - \overline{\varphi}_{i,\mathrm{res}})) + \mathrm{lp\_space}(\overline{\varphi}_{i,\mathrm{res}}) \quad (10)$$

where lp_space ( ) indicates low-pass spatial filtering and hp_time ( ) high-pass temporal filtering. High-pass filtering of $\varphi^k_{i,\mathrm{res}} - \overline{\varphi}_{i,\mathrm{res}}$ will remove the contribution of nonlinear deformation and leave the phases from the decorrelation noise and atmospheric delay of the slave image of the *k*th interferogram. Low-pass filtering of the result will then derive an estimation of the atmospheric phase of the slave image alone. This estimation added by the atmospheric phase of the master image constitutes an estimate of interferometric atmospheric phase.

Subsequently, the phase of nonlinear deformation is retrieved by

$$\varphi^k_{i,\text{non-linear}} = \mathrm{lp\_space}(\varphi^k_{i,\mathrm{res}} - \varphi^k_{i,\mathrm{atm}}) \quad (11)$$

Finally the complete deformation is obtained by adding the above nonlinear deformation to the linear deformation already derived.

4. Recommended procedure of IPTA processing for subsidence mapping

A typical processing flowchart is shown in Fig. 2, illustrating the processing steps associated with the algorithms discussed in previous two sections. Some additional issues, will be discussed in more detail below.

4.1. Quality and density of point targets

The point target candidates can initially be selected by checking the amplitude behavior of each pixel in the time series images. As the deformation information will be retrieved only for those selected points, it is a good practice to have the density of the points as high as possible. Therefore it is unnecessary to set a strict condition for the initial selection of point targets. During subsequent processing, especially in the two-dimensional regression analysis, the quality of a point target candidate can be quantitatively evaluated. For example, for a pair of points (a reference point and another point), the phase increment calculated from the two-dimensional regression analysis may not match perfectly with the actual value in each of the interferograms. The standard deviation of the difference then measures the quality of another point candidate. If the standard deviation of the two-dimensional regression exceeds a

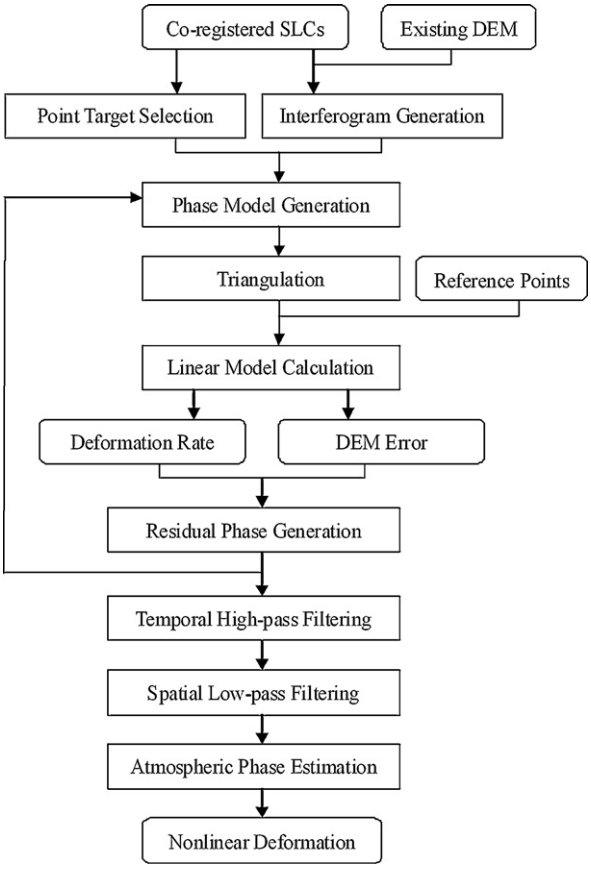

Fig. 2. Procedure of IPTA processing for urban subsidence monitoring.

threshold, e.g., 1.2 rad, the other point of the pair can be regarded as a poor-quality point target, and be removed from the point candidate list.

4.2. Reference point

It is necessary to have at least one reference point where both the DEM error and the linear deformation rate is known, since the result of the two-dimension regression is the relative difference of the interferogram phase of two neighboring points. To get a robust result of the linear phase model, it is better to have a reference point located near the center of the area of interest. If point targets are distributed spatially as several clusters and cannot be connected with arcs shorter than 2 km, more reference points are needed to obtain reliable results.

4.3. Baseline refinement

Another advantage of having more than one reference points is that these points can be used to refine the baseline. Baseline errors can cause a low-frequency phase ramp, often linearly varying in both range and azimuth directions. The phase artifact due to baseline errors shows somehow similar spatial and temporal characteristics to the atmospheric phase. Therefore, we did not single out the phase caused by baseline error in Eq. (1) as Ferretti et al. (2000) has done. The two kinds of phases, however, are different. The atmospheric phase is not expected to show significant linear trends across the whole image as the phase caused by baseline error. This difference is even more significant if a large area is considered (e.g., a full ERS/ENVISAT SAR frame). To achieve a better result, the baselines have to be refined. This can be done based on the relationship between the unwrapped interferogram phase with the topography height and known deformation. So, if there are several reference points (more than 5) available, the baselines can be refined by least-squares fit of known topographic and deformation phases at these points. Otherwise, the baselines can be refined through some stable points. Of course, modification of baseline will compensate for part of phase trend originated from atmospheric heterogeneity. This, however, will not affect the estimation of surface deformation.

4.4. Iteration

Iteration is an integral part of IPTA processing. With iteration, the accuracy of the parameter estimates can be improved step by step. There is not a fixed execution order for the iteration, and the optimal solution may be different from one case to another. In general, iteration can be applied in the following circumstances.

a) To get a first reliable solution of the linear phase model. In the first effort to solve the linear phase model expressed by Eq. (4), we can restrict the calculation only to those interferograms with relatively short baselines, e.g., less than 500 m, to guarantee good coherence over the majority of candidate point targets. It is not expected that the complex valued differential interferogram phases can be unwrapped correctly for every pair of neighboring points on each interferogram because of strong atmospheric distortions and/or large baseline errors. The quality of phase unwrapping can be judged by the smoothness of the residual phase. Note that the relative DEM errors and linear deformation rates are not calculated based on wrongly unwrapped phases. Therefore, the two-dimensional regression analysis needs to be done again for only those correctly unwrapped interferograms. The calculated DEM error and linear deformation rate from this iteration will be a first reliable solution of the linear phase model.
b) To include more interferograms into regression analysis. A first reliable solution calculated based on a subset of available interferograms is followed by the interferogram phase model expressed by Eq. (1). This can be updated by taking the calculated DEM error and linear deformation rate into account. This can be applied to all available interferograms, rather than the subset. Then the 2-D spatial searching algorithm can be iterated. At this time, it can be expected that more interferograms will be correctly phase-unwrapped. For those interferograms still not correctly unwrapped, a spatial phase unwrapping algorithm like minimum cost flow method (Costantini, 1998) can be employed to unwrap the residual phase. Since the large portion of the interferogram phase has been accounted for by virtue of the DEM error and linear deformation rate, the residual phase will show very low frequency spatial variation, therefore can be easily unwrapped. At this point, every interferogram of the original stack can be correctly phase-unwrapped.
c) To update the phase model after baseline refinement. Once the baseline is refined, the phase caused by DEM can be updated, so does the differential interferograms. The two-dimensional regression analysis can be iterated to obtain updated solution.

5. A case study in Suzhou

Suzhou is within the center of the Yangtze river delta region which represents one of the most developed parts in China. The area suffers the most severe ground subsidence mainly caused by over exploitation of underground water. Because it is humid and rainy in Suzhou, the vegetation is relatively dense. Temporal decorrelation on C-band imagery is a big challenge for traditional SAR interferometry. Therefore, the IPTA method is used to map ground subsidence in Suzhou.

Table 1
List of SAR images used in this study.

#	Mission	Date	Temporal baseline (day)	Normal baseline (m)
1	ERS-1	1993-2-25	−1879	358
2	ERS-1	1993-4-1	−1844	296
3	ERS-1	1993-6-10	−1774	−579
4	ERS-1	1993-7-15	−1739	−778
5	ERS-1	1993-8-19	−1704	−440
6	ERS-1	1993-10-28	−1634	405
7	ERS-1	1993-12-2	−1599	558
8	ERS-1	1995-4-29	−1086	−624
9	ERS-1	1995-7-8	−1016	−761
10	ERS-1	1995-12-30	−841	329
11	ERS-1	1996-3-9	−771	311
12	ERS-2	1996-3-10	−770	253
13	ERS-2	1997-8-17	−245	−49
14	ERS-2	1997-9-21	−210	−405
15	ERS-2	1998-2-8	−70	−459
16	ERS-2	1998-3-15	−35	−282
17	ERS-2	1998-4-19	0	0
18	ERS-2	1998-5-24	35	−367
19	ERS-2	1998-6-28	70	−993
20	ERS-2	1998-10-11	175	202
21	ERS-2	1998-11-15	210	170
22	ERS-2	1998-12-20	245	−495
23	ERS-2	1999-6-13	420	−727
24	ERS-2	1999-8-22	490	885
25	ERS-2	1999-9-26	525	425
26	ERS-2	1999-12-5	595	−369
27	ERS-2	2000-1-9	630	−231
28	ERS-2	2000-2-13	665	225
29	ERS-2	2000-4-23	735	792
30	ERS-2	2000-5-28	770	639
31	ERS-2	2000-8-6	840	13
32	ERS-2	2000-10-15	910	317
33	ERS-2	2000-11-19	945	767
34	ERS-2	2000-12-24	980	−576

A total of 34 ERS-1/2 SAR scenes spanning from early 1993 to the end of 2000 have been collected (see Table 1). According to the above-mentioned criterion, the image acquired on April 19, 1998 was selected as the master image. The original SLC data was 5-look processed in azimuth, and a subset covering the whole Suzhou city was used. The DEM was extracted from the 1:50,000 national geospatial database and has 25 m grid size and vertical accuracy of 3.0 m. Fig. 3 shows the average 5-look amplitude image from the 34 scenes.

Initially, 41,838 point target candidates were extracted based on the amplitude dispersion index (see Fig. 4(a)). A point target candidate near the Huqiu hill marked by the yellow triangulation in Fig. 3 was selected as a global reference, because the Huqiu hill is located on a stable geological block and has not been affected by ground subsidence for a long time (Yuan and Zhou, 2001). (For interpretation of the references to color in this text, the reader is referred to the web version of the article.) Also the Huqiu hill is very close to the center of Suzhou. The first solution to the linear phase model expressed by Eq. (4) was derived based on the arcs shorter than 2 km in the triangular irregular network shown in Fig. 4(b). After iterations, 38,881 high quality point target candidates were obtained. Finally, the linear and nonlinear deformation in radar line-of-sight (LOS) direction at those points was retrieved with positive value corresponding to movement away from the sensor. Fig. 5 shows the average deformation velocity which is calculated by dividing the total deformation projected into the up–down direction with the time span. We can see subsidence mainly occurred along the eastern rim of the old city. There are three obvious subsidence zones which are located at the north-eastern, middle-eastern and south-eastern areas of center Suzhou, respectively. The spatial pattern is consistent with the report published by Yuan and Zhou (2001).

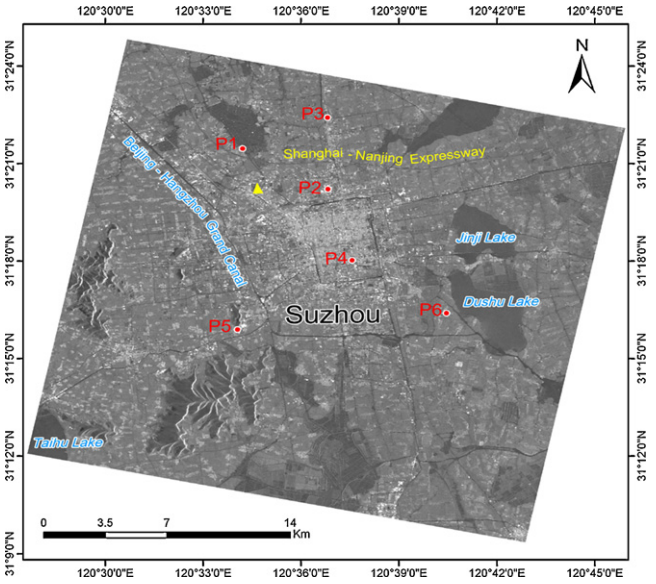

Fig. 3. Average 5-look amplitude of Suzhou, covering an area around 12 (west-east) × 15 km^2. The famous Beijing–Hangzhou Grand Canal winds from North to south in the west of Suzhou, while another important construction, the Shanghai–Nanjing Expressway passes Suzhou in the north. The reference point marked by a yellow triangulation is located near Huqiu hill. The 6 points where we get leveling result are also marked in the image.

To quantitatively validate the IPTA result, we got the record of vertical subsidence amount between January 1992 and December 2000 at 6 point targets from the local geological surveying department. The vertical subsidence amount was derived from leveling measurements. The average annual deformation rate was then calculated and compared with the IPTA result. The comparison is shown in Table 2. The differences are at millimeter level with larger difference corresponding to larger subsidence. The standard deviation is 2.7 mm/a, which suggests that the IPTA result is very accurate. The deformation evolution of the 6 points is shown in Fig. 6. Over exploitation of underground water is the main reason for ground subsidence in Suzhou (Yuan and Zhou, 2001), very similar as the case of Tianjin reported by Zhou et al. (2003). According to Yuan and Zhou (2001), large amplitude ground subsidence started to occur in Suzhou at the beginning of 1980s. From 1990, Suzhou government started to control underground water exploration activities, including closing some wells and refilling water into underground layers, to resist urban subsidence. Underground water level showed a small period of rebound from 1990 to 1991. After that, however, due to the fast industrial development, which stimulated groundwater extraction in the suburban area, underground water level kept steady decline with the lowest level occurred near the end of 1996. The level slowly recovered after that till 1998 due to the second round of water conservation measures taken by Suzhou government. The reference did not provide the information about underground water level after 1998.

Table 2
Comparison of average deformation velocity (mm per year) derived with IPTA technique and leveling measurement.

	IPTA result	Leveling measurement	Difference
P1	−31.9	−30	−1.9
P2	−33.8	−38	4.2
P3	−20	−20	0
P4	−25.2	−24	−1.2
P5	−6.5	−5	−1.5
P6	−33.3	−29	−4.3
RMS	2.69		

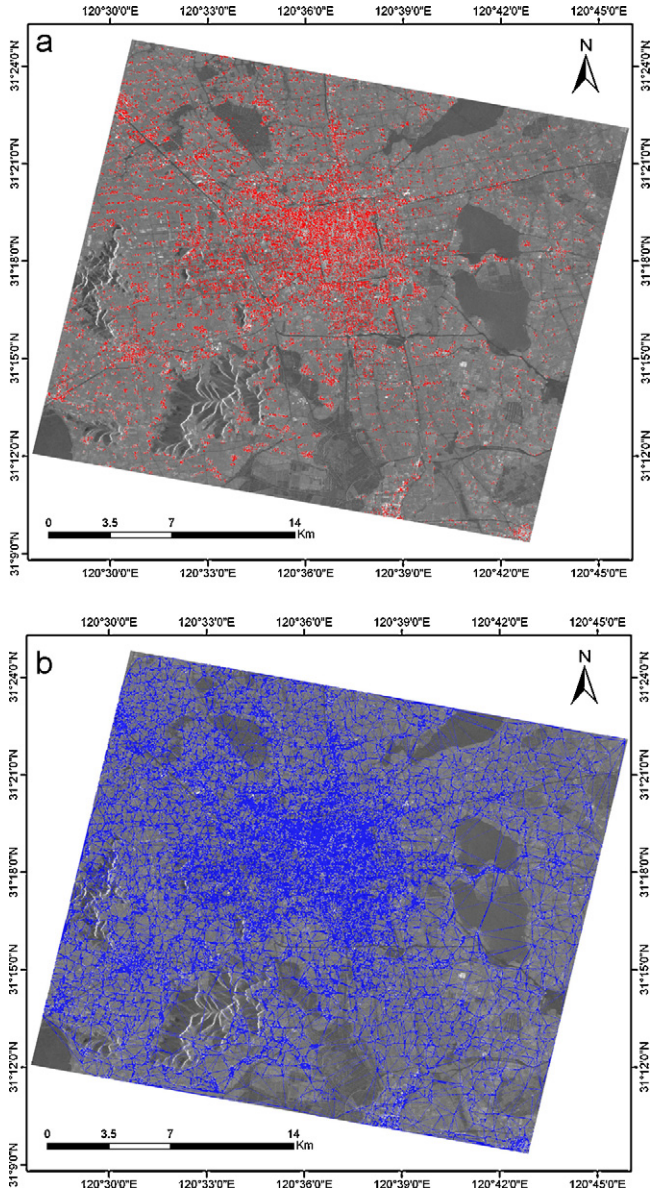

Fig. 4. (a) Selected 41,838 point target candidates using amplitude based criteria and (b) the Delaunay triangulations before removing arcs over 2-km length.

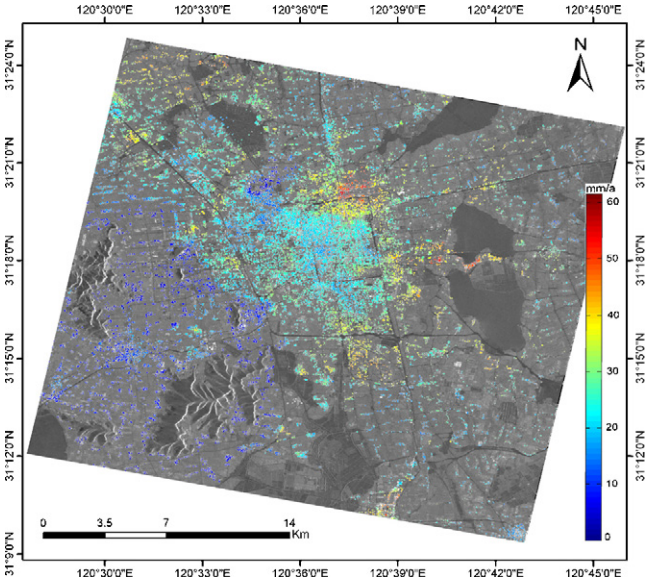

Fig. 5. Average subsidence velocity (mm/year) over 38,881 high quality point targets using the IPTA method and 34 ERS-1/2 SAR images of Suzhou acquired between February 1993 and December 2000. At each point target, the accumulative deformation is calculated by integrating the IPTA derived LOS linear and nonlinear deformation in every time interval and then projected into the up–down direction. The average subsidence velocity is finally obtained by dividing the projected accumulative deformation by the total time separation of 7.83 years.

Correspondingly, from Fig. 6, we can see small scale ground uplift at nearly all points except point 4 from February to August of 1993, steady and steep subsidence followed between 1993 and 1996, and nearly no movement between March 1996 and August 1997. The clear correlation between ground subsidence and underground water level confirms the accountability of groundwater extraction for Suzhou's ground subsidence. Based on this observation, it would be a reasonable expectation that large extent underground water exploitation had occurred between 1998 and 2001.

6. Discussion

This paper describes an operational procedure of using IPTA method to map ground subsidence in urban environments. Key feature of the proposed method is the 2-D spatial searching algorithm to estimate relative linear deformation rate and DEM error, which is very robust and effective. In addition, several important issues including reference point determination, baseline refinement and iteration have been summarized. The case study in Suzhou demonstrates that the proposed procedure can achieve millimeter precision in urban subsidence mapping, thus representing a cost-effective technique to measure and monitor the wide-spread urban subsidence in China.

The proposed procedure requires a large number (e.g., >30) of SAR images, as stated by Ferretti et al. (2001). The so-called small-baseline subset (SBAS) technique proposed by Berardino et al. (2002) can increase the temporal sampling of deformation monitoring by exploiting all available interferograms with small baseline rather than only the interferograms fixed to a common master. This SBAS technique has been developed further by Mora et al. (2003) to estimate DEM error, linear and non-linear deformation and atmospheric artifacts in a similar way as IPTA. The deformation evolution plot generated from 10 small-baseline interferograms formed by only 14 SAR acquisitions can achieve nearly the same accuracy as that from 24 small baseline interferograms formed by 23 SAR images. Therefore, Mora's technique is an option for ground

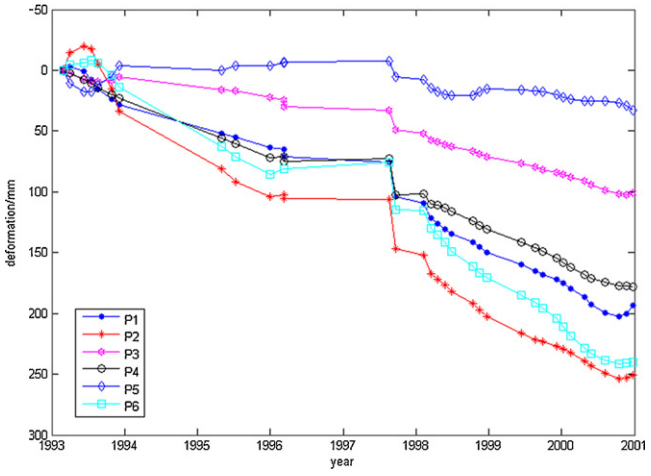

Fig. 6. Deformation evolution of the 6 point targets revealed by IPTA.

subsidence monitoring if there are less SAR images available. In a further study we will apply Mora's technique to a reduced subset of the Suzhou images and compare the result with IPTA.

Nearly all PS related techniques assume that the deformation could be represented as a linear component plus a non-linear component. If the actual deformation severely departs from the linear model, however, Eq. (6) may not hold. In this case, unless higher density of point target and higher coherency level of these point scatterers can be achieved, the derived result may contain large errors (Ferretti et al., 2000; Kampes, 2006). From Fig. 6, the deformation evolution curves of points 1, 2 and 6 suggest that the steady subsidence nearly stopped at the end of 2000, and some small scale uplift occurred again. We may assume that Suzhou government might have taken the third round of water conservation measures to deal with the large amplitude urban subsidence appeared between 1998 and the end of 2000, and the small scale uplift might be the result of the measures. As a further assumption, the urban ground of Suzhou might even steadily uplift thereafter. In such a case, the ground surface deformation scenario after 2001 will be totally different from that during 1992 and 2000 presented in this study. Then the current linear plus non-linear deformation model would be obviously not suitable for this case. Therefore, a more realistic and flexible deformation model is needed to approximate the ground deformations which do not present a simple linear tendency but with relatively complex temporal characteristics.

Acknowledgements

This work has been partly supported by the National Key Basic Research and Development Program, China, under project number 2006CB701303, and the National Natural Science Foundation of China under project number 40571104. The authors would like to thank the anonymous reviews for their constructive comments. The authors are especially grateful to Prof. Alfred Stein of Faculty of Geo-Information Science and Earth Observation of the University of Twente, the Netherlands for review and comments of an earlier draft of this paper.

References

Berardino, P., Fornaro, G., Lanari, R., Sansosti, E., 2002. A new algorithm for surface deformation monitoring based on small baseline differential interferograms. IEEE Trans. Geosci. Remote Sens. 40 (11), 2375–2383.

Costantini, M., 1998. A novel phase unwrapping method based on network programming. IEEE Trans. Geosci. Remote Sens. 36 (3), 813–821.

Dou, X., 2005. Ground deformation: unbearable pain in cities. Express Inform. Mining Ind. 11, 51–55 (in Chinese).

Ferretti, A., Prati, C., Rocca, F., 1999. Permanent scatterers in SAR interferometry. In: Proceedings of IEEE International Geoscience and Remote Sensing Symposium , Hamburg, Germany, June 28–July 2, pp. 1528–1530.

Ferretti, A., Prati, C., Rocca, F., 2000. Nonlinear subsidence rate estimation using permanent scatterers in differential SAR interferometry. IEEE Trans. Geosci. Remote Sens. 38 (5), 2202–2212.

Ferretti, A., Prati, C., Rocca, F., 2001. Permanent scatterers in SAR interferometry. IEEE Trans. Geosci. Remote Sens. 39 (1), 8–20.

Gabriel, A.K., Goldstein, R.M., Zebker, H.A., 1989. Mapping small elevation changes over large areas—differential radar interferometry. J. Geophys. Res. 94, 9183–9191.

Galloway, D.L., Jones, D.R., Ingebritsen, S.E., 2000. Measuring Land Subsidence from Space. USGS Fact sheet-051-00.

Hanssen, R.F., 2001. Radar Interferometry: Data Interpretation and Error Analysis. Kluwer Academic Publishers, Dordrecht, Netherlands.

Jin, J., Pan, M., 2007. Status of land subsidence damages and strategy for disaster prevention and mitigation in China. J. Catastrophol. 22 (1), 117–120 (in Chinese).

Kampes, B.M., 2006. Radar Interferometry: Persistent Scatterer Technique. Springer, The Netherlands.

Lu, Z., Dzurisin, D., Wicks, C., Power, J., Kwoun, O., Rykhus, R., 2007. Diverse Deformation Patterns of Aleutian Volcanoes from Satellite Interferometric Synthetic Aperture Radar (InSAR), in Volcanism and Subduction: The Kamchatka Region. American Geophysical Union Geophysical Monograph Series, vol. 172, pp. 249–261.

Lu, Z., Wicks, C., Kwoun, O., Power, J., Dzurisin, D., 2005. Surface deformation associated with the March 1996 earthquake swarm at Akutan Island Alaska, revealed by C-band ERS and L-band JERS radar interferometry. Can. J. Remote Sens. 31, 7–20.

Massonnet, D., Briole, P., Arnaud, A., 1995. Deflation of Mount Etna monitored by spaceborne radar interferometry. Nature 375, 567–570.

Massonnet, D., Rossi, M., Carmona, C., Adragna, F., Peltzer, G., Feigl, K., Rabaute, T., 1993. The displacement field of the Landers earthquake mapped by radar interferometry. Nature 364, 138–142.

Massonnet, D., Feigl, K., 1998. Radar interferometry and its application to changes in the Earth's surface. Rev. Geophys. 36 (4), 441–500.

Mora, O., Mallorqui, J.J., Broquetas, A., 2003. Linear and nonlinear terrain deformation maps from a reduced set of interferometric SAR images. IEEE Trans. Geosci. Remote Sens. 41, 2243–2253.

Werner, C., Wegmuller, U., Strozzi, T., Wiesmann, A., 2003. Interferometric point target analysis for deformation mapping. In: Proceedings of IEEE International Geoscience and Remote Sensing Symposium, volume VII , 21–25 July, pp. 4362–4364.

Yuan, M., Zhou, W., 2001. Ground subsidence disaster and origin analysis in Suzhou. J. Geol. Hazards Environ. Preserv. 12, 21–24 (in Chinese).

Zebker, H.A., Rosen, P.A., Goldstein, R.M., Gabriel, A., Werner, C., 1994a. On the derivation of coseismic displacement fields using differential radar interferometry: the Landers earthquake. J. Geophys. Res. 99 (B10), 19, 617–619,634.

Zebker, H.A., Werner, C., Rosen, L., Hensley, S., 1994b. Accuracy of topographic maps derived from ERS-1 interferometric radar. IEEE Trans. Geosci. Remote Sens. 32, 823–836.

Zhou, Y., Stein, A., Molenaar, M., 2003. Integrating interferometric SAR data with levelling measurements of land subsidence using geostatistics. Int. J. Remote Sens. 24 (18), 3547–3563.